JOURNAL OF MATERIALS SCIENCE 22 (1987) 2959–2964

Phase equilibria, solidification and solid-state transformations of white cast irons containing niobium

R. KESRI, M. DURAND-CHARRE
Institut National Polytechnique de Grenoble, L.T.P.C.M./E.N.S.E.E.G., BP 75, 38402 St Martin d'Hères, France

Liquid–solid equilibria were studied in the iron-rich corner of the Fe–Cr–C–Nb system, using a combination of several experimental techniques, essentially differential thermal analysis (DTA) and all the usual means of characterization. A modified version of the DTA technique, quench-interrupted DTA, was employed in order to establish the solidification paths. The investigation was focused on the austenitic field for three levels of chromium (15, 9 and 3.5 wt%). The corresponding projections of liquidus in the pseudoternary system are proposed. A slight influence of the other solute contents is found in the case of chromium. The occurrence of blocky NbC carbides depends on the solidification time since it is controlled by a coarsening mechanism.

1. Introduction

Like the other transition elements, niobium forms hard refractory compounds with carbon, boron and nitrogen. The main technical application for these hard compounds is that of niobium carbides in "cemented" carbides where the carbides are cemented with a binder in a hot-pressing or sintering process. In order to improve the understanding of compatibility relations between carbides and metals, many studies have been made concerning the phase diagram of Nb–C [1–3] or the systems NbC–X (X = Fe, Ni, Co or Cr [4]). Another aspect of the problem is that of precipitation in hot-rolled, low-alloyed steels. Small NbC precipitates induce a good strengthening of the materials. At higher temperatures, the same precipitation induces the formation of faceted, square-branched platelets in heavy forgings and steel castings, entailing a severe loss of ductility. This explains why the precipitation of NbC must be severely controlled and has often been studied. The solubility of niobium in austenite has been determined by various authors. A compilation by Strid and Easterling [5] reports all the relations for the solubility products in micro-alloyed steels.

In tool steels, which are the most abrasion-resistant materials currently produced, carbon and alloying elements induce the formation of carbides which are complex carbides of tungsten, chromium, molybdenum, vanadium, niobium and iron. They form during the solidification process mostly as eutectic carbides. Consequently, optimization of the structure has to be examined in relation with data concerning the phase equilibria and crystallization paths. The ternary diagram Fe–Nb–C has never been experimentally investigated, only a hypothetical diagram having been proposed by analogy with the system Fe–Ti–C [6]. Our purpose was to determine the iron-rich corner of the phase diagram for the system Fe–C–Cr–Nb in order to clarify the competition between chromium and niobium as carbide formers during solidification. The mechanical properties of this kind of alloy depend upon the morphology, the nature and the amount of carbides and also the state of the matrix. These characteristics may be discussed in relation with the phase diagram and the thermal history of the alloys.

2. Experimental procedure

Master alloys were melted in a medium-frequency induction furnace under a controlled atmosphere using high purity (> 99.95%) charge materials. Intermediate compositions were prepared from these alloys by button melting in an argon arc furnace. In all, a total of about 30 alloys were studied, in the composition ranges 1.6 to 3.6 wt % C, 3.6 to 15 wt % Cr and 1 to 7 wt % Nb.

The temperatures of phase transformation were determined by differential thermal analysis (DTA) on specimens of mass about 2 g. Heating and cooling were carried out under argon at a rate of $300^\circ C\,h^{-1}$. Another method employed was to monitor solidification occurring under controlled conditions in the DTA furnace and to quench the specimen at a precise moment, either on attainment of the liquidus surface or on the appearance of a eutectic (QDTA). This technique was coupled with quench-interrupted solidification experiments (QIDS) in which the solid–liquid interface configuration is frozen in by rapid cooling, enabling the solidification sequence to be determined.

Optical micrographs were taken on polished sections etched in Murakami or Villela reagent. Deep etchings were made electrolytically using a solution of 10% perchloric acid in acetic acid under 6 V.

Electron probe phase analysis was carried out using

0022–2461/87 $03.00 + .12

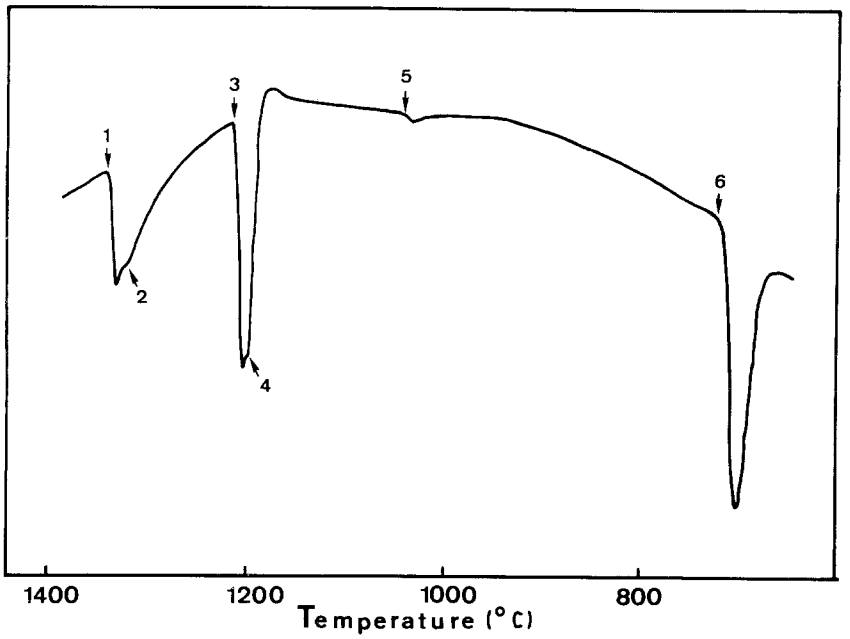

Figure 1 Thermogram for alloy 25. The arrows indicate the corresponding transformations: (1) primary crystallization, (2) formation of the NbC–A eutectic, (3) formation of the M_7C_3–A eutectic, (4) formation of the M_3C–A eutectic, (5) order–disorder transition in NbC carbide, (6) pearlite formation.

an accelerating voltage of 10 kV for niobium and 20 kV for other metallic elements, and subsequent application of a ZAF correction program (atomic number, absorption and fluorescence).

The crystallographic structures were examined by transmission electron microscopy (TEM) on thin foils. Thinning of the foils was done mechanically and then electrolytically under 12 V at room temperature, using the same solution as for deep etching. TEM examinations were made with a Jeol 200 CX microscope.

3. Results

The transformation temperatures, determined by DTA experiments, are given in Table I. Most thermograms display several discontinuities in the solidification range. Fig. 1 gives an example for Alloy 21. Quenching under controlled solidification permitted the identification of the crystallization process corresponding to each accident. The temperature labelled (1) corresponds to primary austenite, temperature (2) corresponds to the NbC–austenite eutectic. Temperature (3) is the formation of the M_7C_3–austenite eutectic (M = metal) and (4) is the formation of the M_3C–austenite eutectic. The liquidus temperature of primary NbC carbides could not be established by DTA experiments. The solidification interval ΔT is reported in Table I. It represents the difference between the liquidus temperature and the temperature at which complete eutectic crystallization is achieved, i.e. a temperature 10 to 15° C lower than the start of the last eutectic crystallization process. Assuming a cooling rate of 300° C h^{-1}, we may relate this interval to a solidification time (Table I).

Five phases were found at the first stage of solidification in the ranges of composition that we studied. They are ferrite, austenite, NbC, M_7C_3 and M_3C carbides. The sequence of solidification is indicated in Table I. The identification of the primary phases was made on the basis of the micrographs of quenched (QDTA) specimens. The discrimination between primary delta ferrite and primary austenite was rather easy, since in the latter case a pearlitic or martensitic transformation is always present.

Identification of primary NbC carbides is not so evident. Coarse NbC carbides are observed with different shapes; some are blocky cuboids more or less grouped in a dendritic structure (Fig. 2); some are faceted octahedrons (Fig. 3). An alloy, previously identified as hypoeutectic, was unidirectionally solidified. The resulting morphologies along the rod are shown in a schema (Fig. 4). The bottom of the rod presented austenite dendrites and the M_7C_3–austenite eutectic with a few NbC cuboid carbides embedded in austenite or located in the interdendritic groove. The amount of blocky carbides increases with niobium and carbon content in the initial alloy. The interface may be defined by the change of size of the austenite dendrites. It is nearly hidden by a crowd of piled-up blocks of carbides accumulated in the mushy zone (Fig. 3). In the upper part of the rod there are smaller dendrite (about 1/10th the size of the other dendrites), the eutectic M_7C_3–austenite, and small blocky carbides scattered in the interdendritic grooves. For the DTA experiments, more cuboid carbides are observed at the top of the small ingot than at the bottom. In the

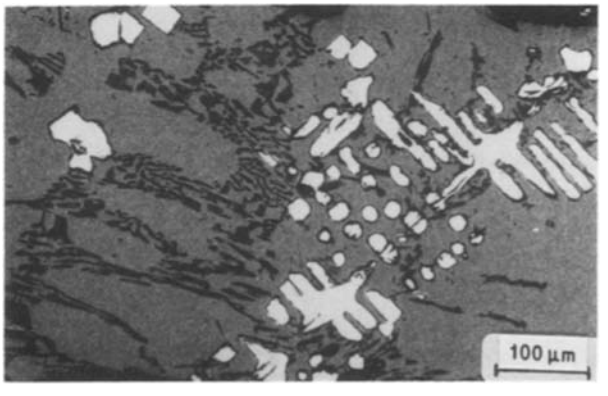

Figure 2 SEM micrograph for Alloy 38 showing primary NbC dendrites (light contrast), austenite dendrites and M_7C_3 (dark contrast) eutectic carbides.

TABLE I Compositions of alloys, partitioning coefficient for chromium at liquidus temperature (k_{Cr}), transformation temperatures, interval of solidification (ΔT) and phases identified in order of their formation during solidification

Alloy No.	Composition (wt %)			k_{Cr}	Transformation temperatures (°C)	ΔT	Solidified phases
	C	Cr	Nb				
10	1.6	3.4	1.0	0.85	1410, 1356, 1138	286	A, NbC–A, M_3C–A
11	1.5	3.3	3.9	0.91	1417, 1395	297	A, NbC–A
12	1.5	3.3	7.0		1424#	309	NbC, NbC–dF
13	2.5	3.5	1.0	0.78	1337, 1270, 1149	211	A, NbC–A, M_3C–A
14	2.5	3.4	3.8	0.80	1363, 1346, 1156	225	A, NbC–A, M_3C–A
15	2.5	3.4	7.0	0.88	1387, 1371, 1169	244	NbC, NbC–A, M_3C–A
16	3.4	3.5	1.0		1247#, 1135	142	A, NbC–A, M_3C–A
17	3.5	3.5	4.0		1276, 1249, 1140	165	NbC, NbC–A, M_3C–A
18	3.5	3.5	7.0		*, 1292, 1141	172	NbC, NbC–A, M_3C–A
20	1.5	9.3	1.0	0.79	1400, 1340, 1225#	185	A, NbC–A, M_7C_3–A, M_3C–A
21	1.6	8.6	3.8	0.85	1400#, 1229#	192	A, NbC–A, M_7C_3–A, M_3C–A
22	1.6	9.0	7.0	0.90	1407, 1239#	193	dF, NbC–A, M_7C_3–A, M_3C–A
23	2.2	9.2	0.6		1363#, 1201#	175	A, NbC–A, M_7C_3–A, M_3C–A
24	2.3	9.4	1.0	0.69	1334, 1283, 1201#	177	A, NbC–A, M_7C_3–A, M_3C–A
25	2.3	9.2	4.1	0.78	1343, 1326, 1205#	177	A, NbC–A, M_7C_3–A, M_3C–A
26	2.3	9.0	7.0	0.83	1361, 1334, 1221#	178	NbC, NbC–A, M_7C_3–A, M_3C–A
27	3.1	8.6	1.0		1252#, 1169, 1154	118	A, NbC–A, M_7C_3–A, M_3C–A
28	3.3	9.0	7.0		*, 1286#, 1192#	142	NbC, NbC–A, M_7C_3–A, M_3C–A
29	3.4	9.8	4.4		1269, 1183#	136	NbC, NbC–A, M_7C_3–A, M_3C–A
30	1.3	15.3	1.0	0.79	1390, 1323, 1252	151	A, NbC–A, M_7C_3–A
31	1.4	14.9	3.9	0.86	1390#, 1251	150	A, NbC–A, M_7C_3–A
32	1.6	14.5	7.0	0.95	1397, 1387, 1350, 1259	150	NbC, NbC–dF, NbC–A, M_7C_3–A
33	2.1	14.7	1.0	0.74	1332, 1232, 1213	151	A, NbC–A, M_7C_3–A
34	2.1	15.0	4.0	0.75	1333#, 1233#	148	A, NbC, NbC–A, M_7C_3–A
35	2.3	14.6	7.0	0.83	1354, 1246	150	NbC, NbC–A, M_7C_3–A
36	2.8	14.1	1.0		1246#, 1210	90	A, NbC–A, M_7C_3–A
37	2.9	14.4	4.1		*, 1263, 1216	93	NbC, NbC–A, M_7C_3–A
38	3.0	14.6	7.0		*, 1279, 1218	101	NbC, NbC–A, M_7C_3–A

= Large peak probably corresponding to several transformations.
* = Undetermined temperature for primary crystallization of NbC carbides.
A = Austenite.
dF = Delta-ferrite.

case of the hypoeutectic alloy, the bottom exhibits austenite dendrites as shown in Fig. 2. For some compositions that we locate in the NbC primary field the QDTA samples exhibited well-formed characteristic NbC dendrites uniformly distributed. However, both kinds of dendrite often coexist (Fig. 2) and then it is difficult to discriminate which one really grew first. In order to establish the primary fields in the projection of the liquidus surface, we have taken into account the microstructures of quenched samples and the liquidus temperatures.

Fig. 5 illustrates the morphology of the NbC–austenite eutectic for Alloy 21 which has been quenched at the liquidus temperature. The eutectic cells are constituted of carbide rods in an austenitic matrix. When the alloys are cooled at a rather slow rate

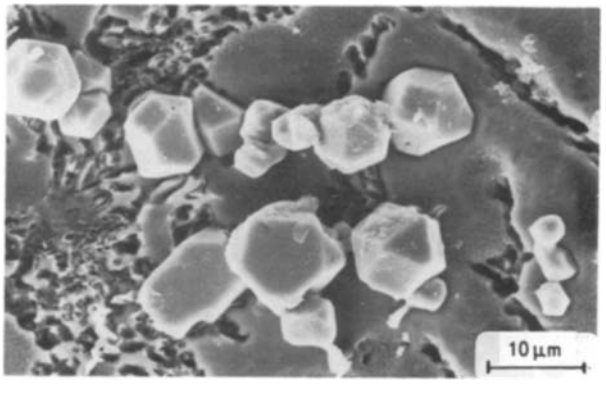

Figure 3 SEM micrograph for Alloy 30 showing coarsened NbC carbides entrapped in austenite or between secondary arms of austenite dendrites.

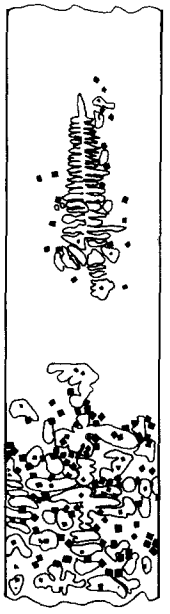

Figure 4 Schematic view of a rod unidirectionally solidified and then quenched, for Alloy 30. The top of the schema represents the as-quenched dendritic interface; the bottom represents the coarsened structure of dendrites with the accumulation of NbC carbides.

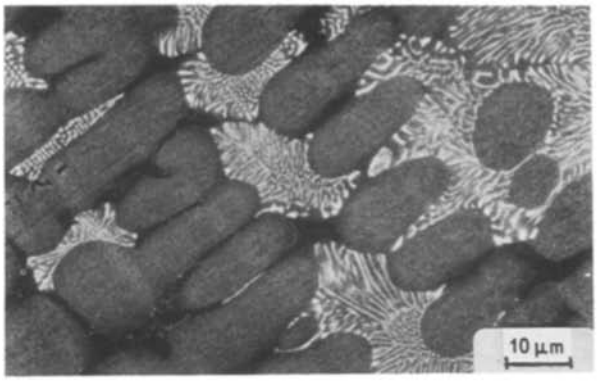

Figure 5 SEM micrograph for Alloy 21 showing austenite dendrites, NbC–A eutectic (light contrast) and the M_7C_3–A eutectic (dark contrast) located between the secondary arms of dendrites.

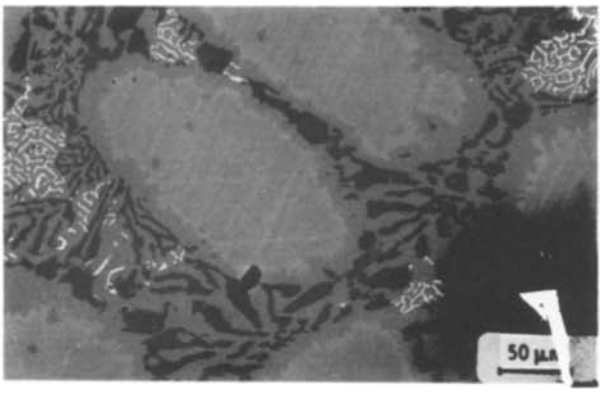

Figure 7 SEM micrograph for Alloy 33 cooled at 150° C h^{-1}, showing M_7C_3–A eutectic and "chinese script" NbC–A eutectic in the interdendritic groove.

(300° C h^{-1}), they exhibit a coarser and angular morphology known as "chinese script" (Figs 6 and 7). The eutectic formed with M_7C_3 complex chromium–iron carbides and austenite appears in the interdendritic groove. The microstructure observed for the M_7C_3–austenite eutectic is characteristic of spade-like carbides; the same is true for the M_3C–austenite eutectic with a ledeburitic aspect. The projection of the liquidus surface for the three levels of chromium, presented in Fig. 8, takes into account the results concerning the primary phase fields and the crystallization paths.

Two peaks in the thermogram (Fig. 1) correspond to solid-state transformations. In all the alloys there is a transformation at a temperature of about 1025° C which corresponds to the small peak labelled (5) on the thermogram. The same thermal discontinuity was found in the DTA thermogram for synthetic NbC carbide powder and was attributed to the order–disorder transformation. The peak labelled (6) corresponds to the pearlitic reaction; it is often a large flattened peak ranging between 715 and 675° C. This pearlite has a very small interlamellar spacing and is difficult to observe. From examination of a thin foil this spacing can be estimated at 0.1 µm for a sample cooled at 300° C h^{-1}.

We analysed the niobium content in the matrix: it is very small. We could just estimate the concentration at about 0.05 at %. We determined the proportion of different metals in the different kinds of carbide. NbC carbide do not contain any substitutional element, while M_7C_3 and M_3C contain a very small amount of niobium. The formulae of these two latter carbides are respectively $(Cr_{0.51}Fe_{0.49})_7C_3$, $(Fe_{0.88}Cr_{0.12})_3C$. We determined the partitioning coefficients of chromium k (Table I) between the liquid and the austenite or the ferrite by analysis of the centres of the dendrites. The values obtained range close to 0.75 for k in austenite and close to 0.89 in ferrite. There is a slight influence of the carbon and the niobium contents: niobium increases the value of k and carbon decreases it. We represent this variation by an equation of the first order which enables the coefficient to be interpolated in the austenitic field:

$$k_{Cr}^{A} = 0.761 - 0.098[X(C) - 2] - 0.007[X(Cr) - 10] + 0.010X(Nb)$$

X_i being the i wt % content.

In samples quenched from the liquidus temperature we identified for the NbC carbides the cubic pattern of the disordered structure (Fig. 9). However, in slowly cooled samples we identified a hexagonal structure corresponding to the long-range-order structure based on Nb_6C_5 (or $NbC_{0.83}$) for the chinese-script carbides located in the eutectic NbC–austenite. This ordered structure was found only in slowly cooled or annealed samples. In the samples containing less carbon, the same diffuse electron scattering as for VC_x, revealing a tendency to a short-range order as in $VC_{0.75}$, was observed [7]. As carbon analysis is difficult to perform in small precipitates, the identification of the ordered structure indicates the corresponding composition. This part of the investigation is developed separately [8].

The growth direction of the carbides was not determined precisely. However, we indicate that in the case of the branches of "chinese script" it was near ⟨0 0 1⟩ (Fig. 10).

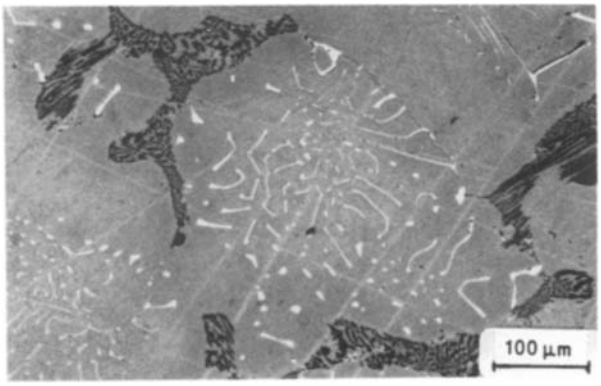

Figure 6 SEM micrograph for Alloy 32 cooled at 300° C h^{-1}, showing pearlitic matrix, "chinese script" NbC–A eutectic and M_7C_3–A eutectic.

4. Discussion and conclusions

The main problem was to locate the primary field boundary between austenite and NbC carbide. In fact, the occurrence of large carbide precipitates is not sufficient evidence that the corresponding com-

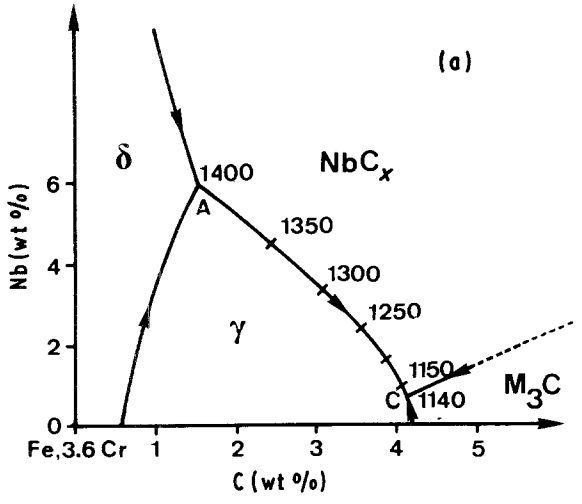

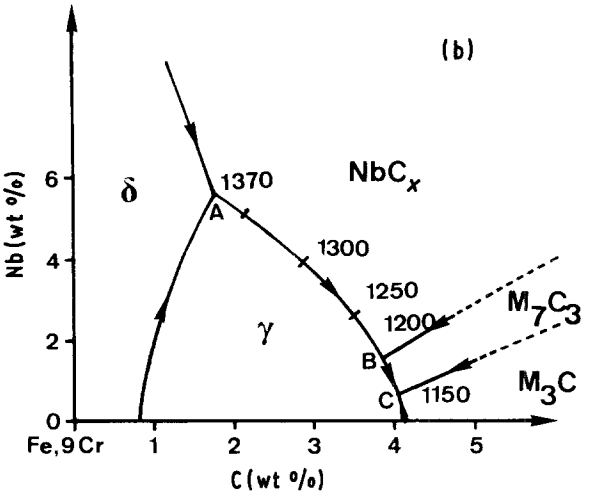

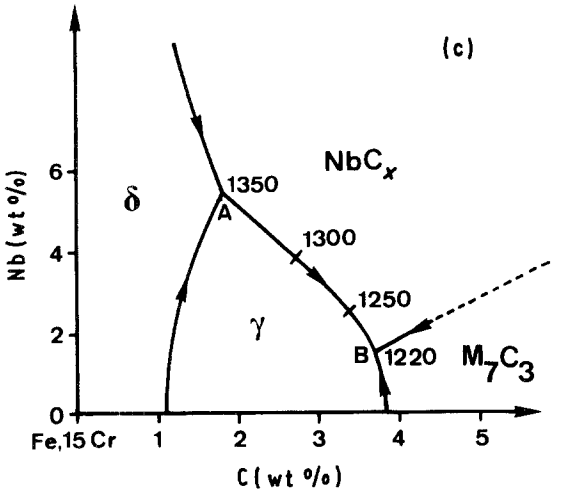

Figure 8 Projection of liquidus for the pseudoternary system (Fe–Cr)–Nb–C with three levels of chromium: (a) 3.5, (b) 9, (c) 15 wt %.

position falls in the primary NbC field. The formation of these carbides is dependent on the solidification rate. Bhambri *et al.* [9], studying a superalloy containing niobium and carbon, also found different morphologies for the MC carbides depending on the growth conditions. These authors explain the formation of faceted carbides by a mechanism of coarsening of MC nuclei pre-existing in the melt. During our DTA experiments, marked superheating was avoided, so some particles may never have dissolved.

The problem of remaining particles acting as nuclei in the melt has often been brought up in the case of NbC carbides. To coarsen, these particles need time and a supply of solute. Time is related to the solidification range ΔT, which is indicated in Table I for a cooling rate of $300^\circ C\,h^{-1}$. This gives an indication of the time during which coarsening operates for a motionless particle. During solidification, solute will accumulate in an enriched layer moving ahead of the interface. There is a large excess of niobium rejected from the solid due to its very small partitioning coefficient. The thickness of the boundary layer is inversely proportional to the growth rate. In the case of steady-state conditions it might be estimated at about 200 μm, which is the same order of magnitude as the interdendritic spacings. For our experiment of unidirectional solidification (Fig. 4) steady-state

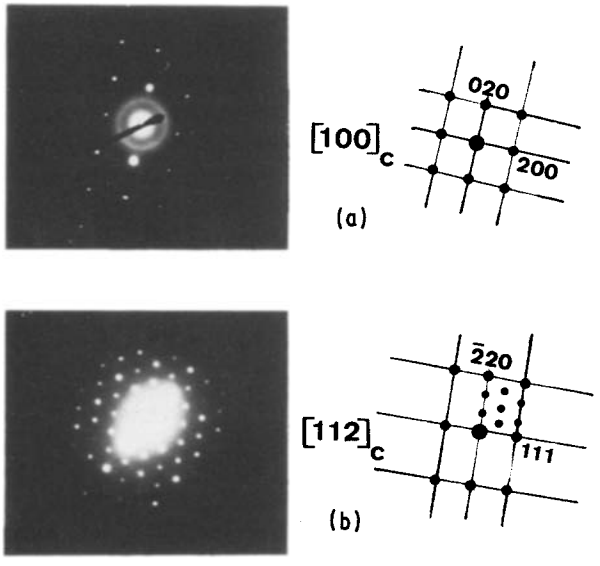

Figure 9 Electron diffraction pattern of NbC carbides: (a) disordered structure corresponding to as-quenched alloys, (b) superlattice Nb_6C_5 corresponding to slowly cooled alloys. Directions of the cubic cell are indicated.

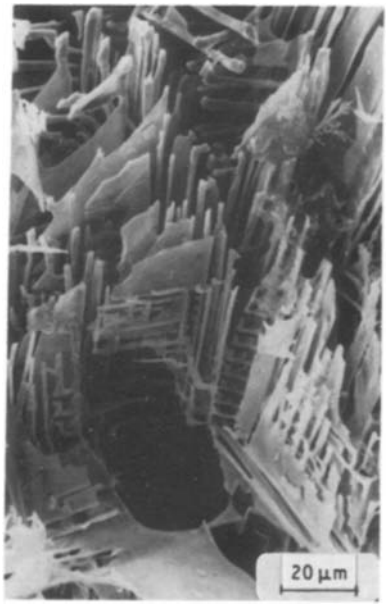

Figure 10 SEM micrograph for Alloy 33: deep etching on as-quenched sample, showing the right-angle branching of NbC eutectic carbides.

conditions were not reached, since an accumulation of carbides was observed at the interface. However, we may assume a niobium-enriched layer extending in the interdendritic groove where the liquid is more confined. The increase of solute probably induces a constitutional supercooling which facilitates the coarsening of particles. The carbon needed for the carbide formation is removed easily from the melt on account of its high diffusivity. The calculated density of NbC carbide is 7.4; the density of the initial melt may be estimated a little higher. The difference is not sufficient to induce a rapid upward motion of the particles in the melt. The increase of solute corresponds to an increase in the density of the liquid. So, whenever the free carbide particles collide with the interface, they are pushed away by the dense layer. Sometimes these particles are caught by the faster moving interface. In Fig. 3 some smaller particles are observed near the centre of the dendrite; they have been entrapped at the early stage of their coarsening. Fernandez *et al.* [10] confirmed that this type of MC carbide grows from the liquid and that their size increases with decreasing cooling rate.

The liquidus projection (Fig. 7) appears to be very similar to that established by De Mello and Durand-Charre in the case of Fe–C–Cr–V alloys [11]. The initial niobium content must exceed a certain amount in order to allow the crystallization of eutectic niobium carbides. The extension of the austenite field is more limited than for vanadium alloys. This can be related to the lower solubility of niobium in austenite. Another difference consists in the nature of the four-phase reaction between austenite, NbC (or VC), M_3C and liquid and between austenite, NbC (or VC), M_7C_3 and liquid. In the case of vanadium the reactions are pseudo-peritectic. In the case of niobium they are either eutectic or there is a tendency for them to become peritectic if their chromium content is higher than 15 wt %. Chromium raises the liquidus temperature in both cases, but this effect is stronger in vanadium alloys. For compositions close to the ternary eutectic composition, no ternary microstructure could be observed, even on thin foils of quenched samples. Considering the barycentre rule applied to the triangle of tie-lines joining the compositions of NbC, M_3C and austenite it appears that the NbC content should be very small. Consequently this phase probably cannot form.

The crystallization paths determined for hypoeutectic alloys appeared to be very similar to those indicated for vanadium alloys. At high solidification rates the microstructures are also similar, with cells of NbC rods (Fig. 4). This diagram provides a basis for discussion of the formation of either M_7C_3 or MC carbides in tool steels. In effect, the wear rate is related to the amount, the nature and the morphology of the carbides [12–14]. However, the whole crystallization process cannot be interpreted only with the pseudo-ternary liquidus projection. For instance, in the case of the alloy shown in Fig. 6a, the "chinese script" structure of the NbC–austenite eutectic may be found in the middle of the interdendritic groove. The initial chromium content is high, so the M_7C_3–austenite eutectic forms first. These same phases segregate niobium, inducing finally the formation of NbC.

Two morphologies are distinguished: one is the so-called "chinese script". This morphology consists of an intricate pattern of plates set at right-angles, usually mentioned for niobium alloys. Our estimation of crystallographic orientations agrees with the results of Riedl *et al.* [15]. The other morphology occurs with quenched samples. It is rather similar to that obtained for the eutectic cells of VC–austenite [11]. The VC rods are less branched, the interlamellar spacing is smaller and branching does occur at right-angles.

The ordering of the NbC phase does not give as many structures as in the case of vanadium alloys. The structure Nb_6C_5, similar to V_6C_5, was found but the transformation is not so easy. The V_6C_5 structure was less brittle than the other VC_x structures [16] on account of a larger cleavage surface energy, which suggests an extremely low mobility of dislocations in the material. However, the brittleness of the material does not depend essentially on the intrinsic brittleness of the carbide but more on the cohesion between the matrix and the carbides. The platelets are responsible for brittle intergranular fractures. They do not crack during fracture but during the cooling process, on account of differential thermal shrinkage between the matrix and the carbides [10].

References

1. E. K. STORMS, "The refractory carbides", edited by J. L. Margrave (Academic, New York and London 1967) p. 61.
2. E. RUDY, St. WINDISCH and C. E. BRUKL, "Planseeberichte für Pulvermetallurgie", Vol. 16 (1968) p. 3–33.
3. B. ARONSON and L. J. ASCHAN, in Proceedings of the International Symposium "Niobium 81", San Francisco, California, November 1981, edited by H. Stuart (Metals Society of AIME, 1984) pp. 637–652.
4. J. P. GUHA and D. KOLAR, *J. Less-Common Metals* **29** (1972) 33.
5. J. STRID and K. E. EASTERLING, *Acta Metall.* **33** (1985) 2057.
6. N. E. HANNERZ, U. LINDBORG, and B. LEHTINEN, *J. Iron Steel Inst.* **68** (1968) 68.
7. J. BILLINGHAM, P. S. BELL and M. H. LEWIS, *Acta. Crystallogr.* **A28** (1972) 602.
8. R. KESRI and S. HAMAR-THIBAULT, *Acta Metall.* to be published.
9. A. K. BHAMBRI, T. Z. KATTAMIS and J. E. MORRAL, *Metall. Trans.* **6B** (1975) 523.
10. R. FERNANDEZ, J. C. LECOMTE and T. Z. KATTAMIS, *ibid.* **9A** (1978) 1381.
11. J. D. B. De MELLO and M. DURAND-CHARRE, *Mater. Sci. Engng.* **67** (1984) 109.
12. H. BERNS and W. TROJAHN, *Z. Werkstofftech.* **14** (1983) 382.
13. E. T. MAKRAY, E. B. FILHO and A. M. MARTINEZ NAZAR, *Metalurgia-ABM* **39** (1983) 665.
14. S. R. KEOWN, E. KUDIELKA and F. HEISTERKAMP, *Met. Technol.* (1980) 50.
15. R. RIEDL, S. KARAGOZ and H. FISCHMEISTER, *Z. Metallkde* **74** (4) (1983) 199.
16. R. K. GOVILA, *Acta Metall.* **20** (1972) 447.

Received 30 September 1986
and accepted 16 January 1987